Supplementary Data

Validating Hierarchical Model Synthesis

For modeling lattice assemblies with finite elements, we claim that models can be calibrated by using simple tests of modular parts and synthesized into accurate models of large assemblies. We validate some of this claim here, but more details can be found in Calisch.[27]

In Supplementary Figure S1, we show results from testing a set of milled phenolic parts of varying cross-sectional dimensions. These parts assemble by using a simple clip to create a cuboct lattice. Across the values of strut widths, we show that a single choice for a radius of rigidity around the nodes fits the data well (whereas a naïvely implemented meshed model does not).

These same parts are assembled into two larger test structures: a $3\times3\times3$ cell brick for compression tests (Supplementary Fig. S2) and a $10\times2\times2$ beam for bending tests (Supplementary Fig. S3). The same beam-based finite element model as described in this work is used to simulate the lattice behavior, and the value for the rigid radius parameter is chosen by using the calibration tests described earlier. In both load cases, the results from Frame3dd matched the experimental data to within 10%.

Flexural Lattice Design

As illustrated with the wing prototype, actuators can be used to safely limit structural deformation that is made possible by designed compliance. Another strategy involves modifying struts and lattice geometries to exhibit high bulk strain at low material strain, making use of geometric nonlinearity. This type of ''flexure'' design is common in mechanical design and can be adapted here to our lattice structures. As an example,

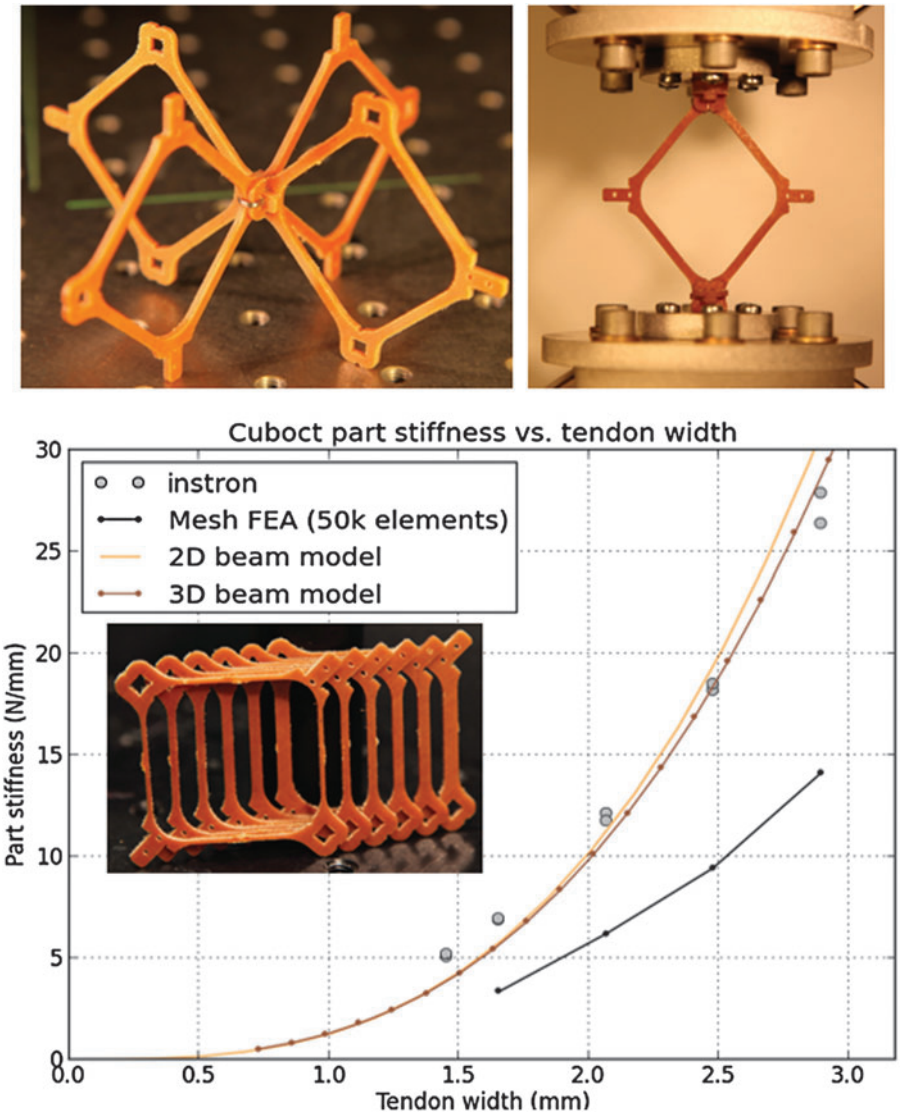

SUPPLEMENTARY FIG. S1. Calibrating models of modular parts. Testing of milled phenolic composite parts with strut widths ranging from 1.5 to 3.0 mm.

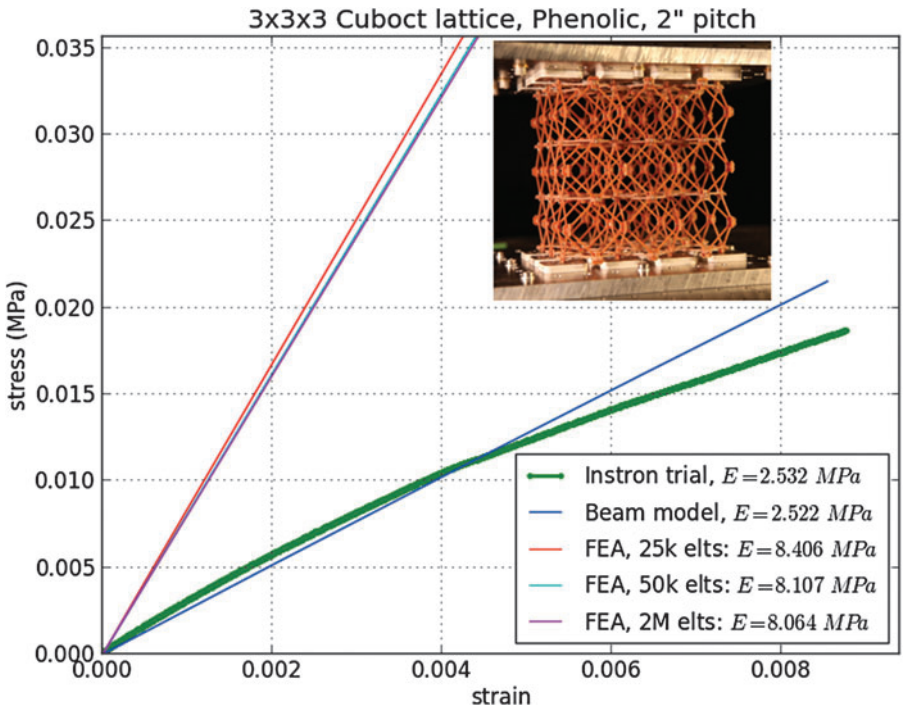

SUPPLEMENTARY FIG. S2. Comparing measured, beam, and FEA modeled moduli for compression. The beam model is closer to experimental data than FEA. FEA, finite element analysis.

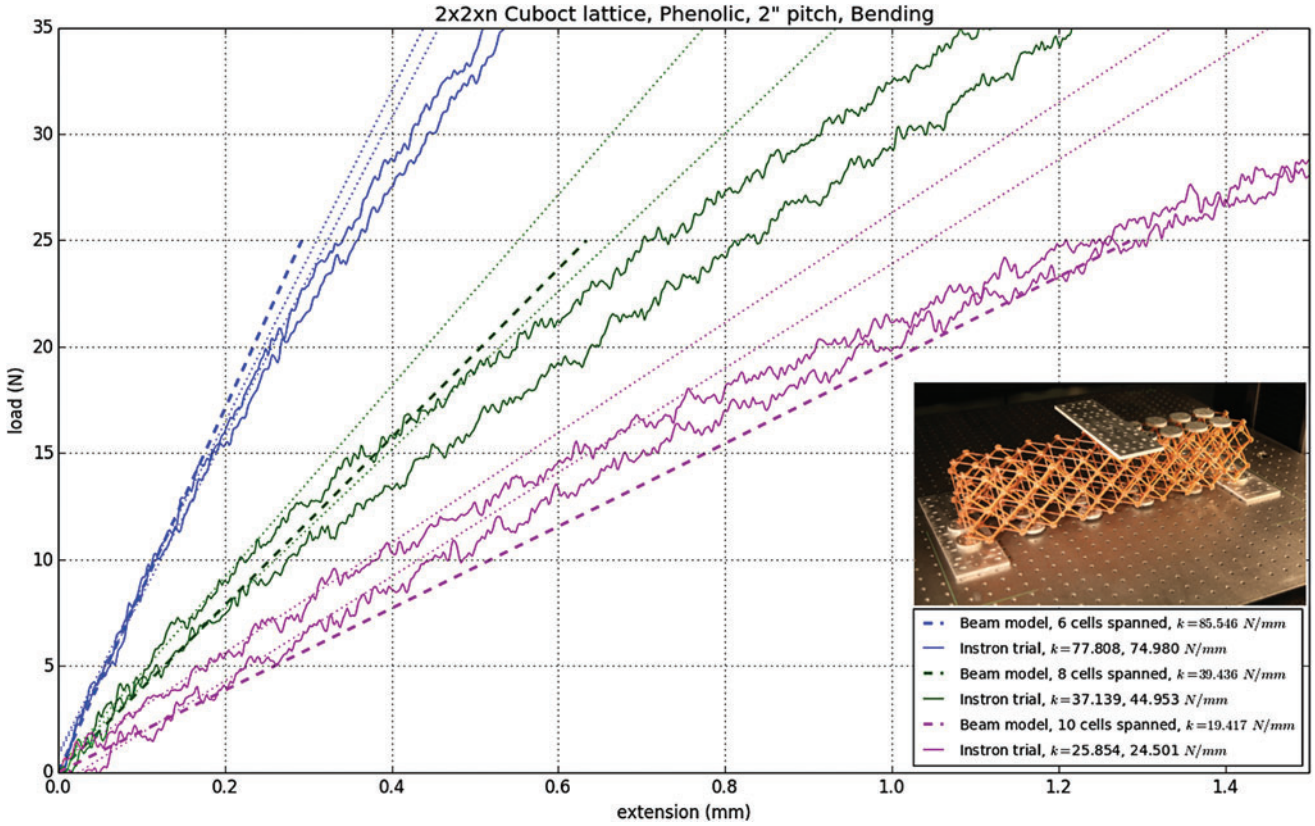

SUPPLEMENTARY FIG. S3. Comparing measured versus beam modeled moduli for bending. This comparison shows that the beam model matches experimental data.

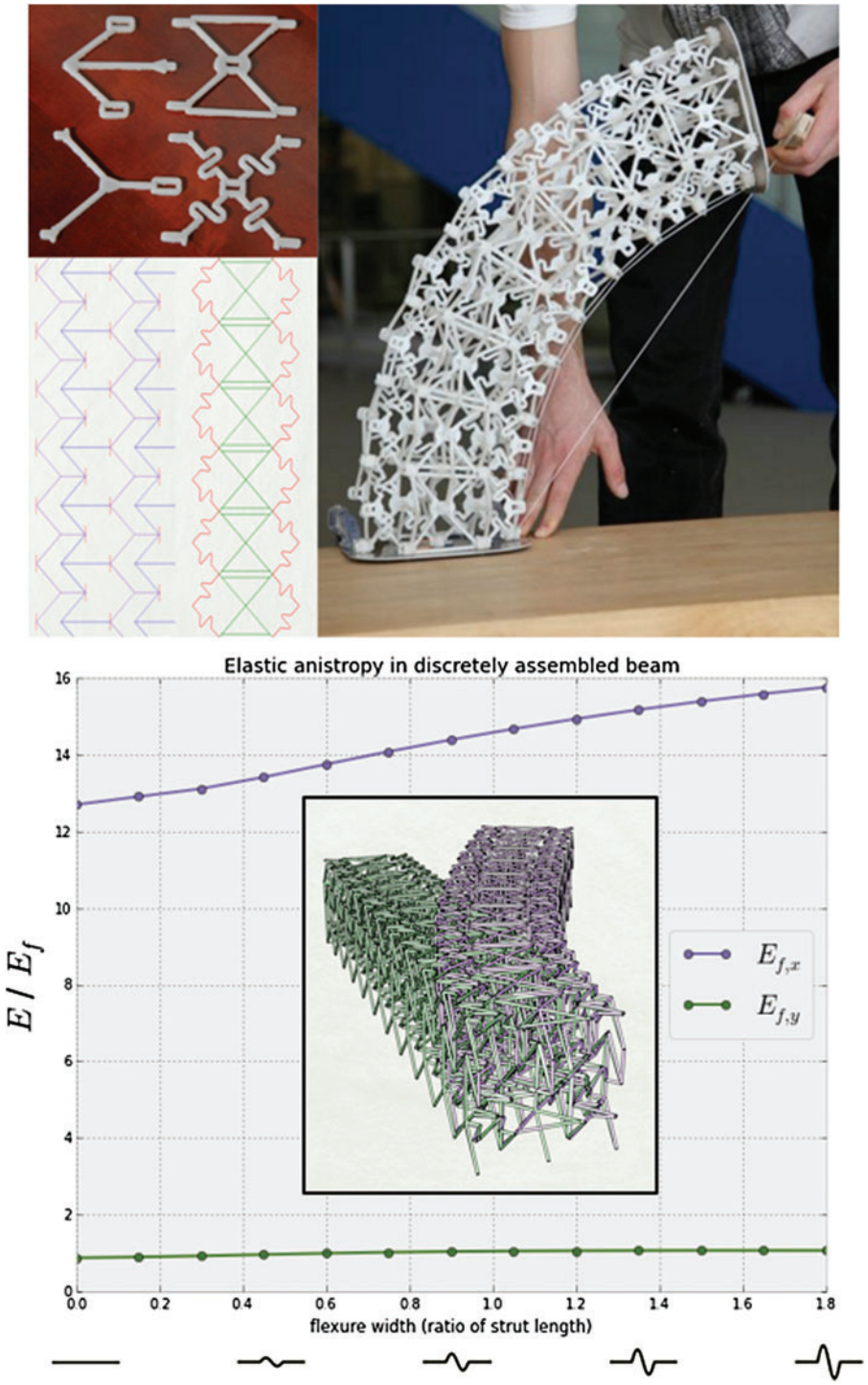

SUPPLEMENTARY FIG. S4. Experimental zero Poisson structure designed for anisotropic bending with low material strain.

consider the lattice shown in Supplementary Figure S4. Four part types are assembled into a structure that is highly compliant in bending along one axis (reversibly bending through 90°), while being relatively rigid in compression and in bending along the other axis. This is possible, because the lattice formed by the struts is carefully designed based on the geometry of zero-Poisson ratio networks.[30] The simulations show that bending in the stiff direction is nearly as stiff as the bulk tensile modulus, whereas bending in the compliant direction is roughly 15 times more compliant.

Supplementary Figure S5 shows an artist's conception using these anisotropic, compliant lattices to make discretely assembled legged robots. Actuated internally with tendons, this system produces lifelike gaits by using flexural deformation.

Wing Experiment Platform Details

Construction details can be seen in Supplementary Figures S6–S8. We can observe small effects of wrinkling under static loading. However, under dynamic loading, the wrinkling

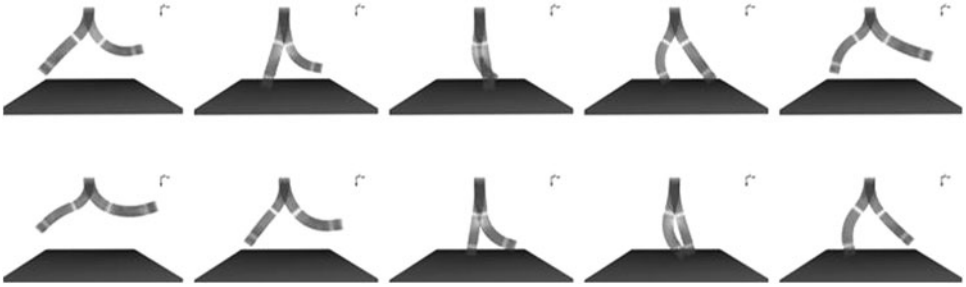

SUPPLEMENTARY FIG. S5. Discretely assembled morphing legs. Artist's conception for high-performance legged robots using only elastic deformation.

pattern is altered due to positive and negative pressures being applied (Supplementary Fig. S9). This wrinkling may exacerbate the effects of ventilation, as discussed in the next section. Future testing will investigate discrete skin panels, as opposed to strips, to closer approximate the morphing surface.

Parasitic Drag Inspection

One theoretical advantage of an active twist system is the potential drag reduction, but we saw in these experiments that the traditional model had lower magnitudes of drag. This is even the case for the flat configurations where there is no twist or flaps, which suggest that the difference between the two is the parasitic drag. We estimated the parasitic drag as the drag at the point where there is no lift.

We can see from Supplementary Figure S10 that the rigid model had a much lower parasitic drag coefficient than either of the flexible models, but the Flex 2 model has a lower parasitic drag than the Flex 1 model. The two flex models are identical in the form of their construction and geometry; the primary difference is that the Flex 2 model had all of the reversible joints and attachment points glued. This did not seem to have any visual difference, but it appears that it had a quantifiable difference in force response. During testing, it is clear that the Kapton strips used for the skin on the flexible models fluttered and likely resulted in ventilation. It seems likely that the skin selection is a large contributing factor in the increase of the parasitic drag.

It is likely that skin friction has a dominant effect on the difference in the flat parasitic drag; however, when the flap is actuated or the tip is twisted, there is a change in the form friction. We can estimate this by assuming that the skin friction is nearly the same for each configuration and by looking at the difference in parasitic drag.

Supplementary Figure S11 shows the difference in parasitic drag for the flaps and active twist. Overall, the difference in parasitic drag is small for the active twist configurations. When we compare the two most similar configurations, the *6° Tip Twist* and *10° Flap*, we see that the magnitude of change for the flex models are nearly half that of the flaps.

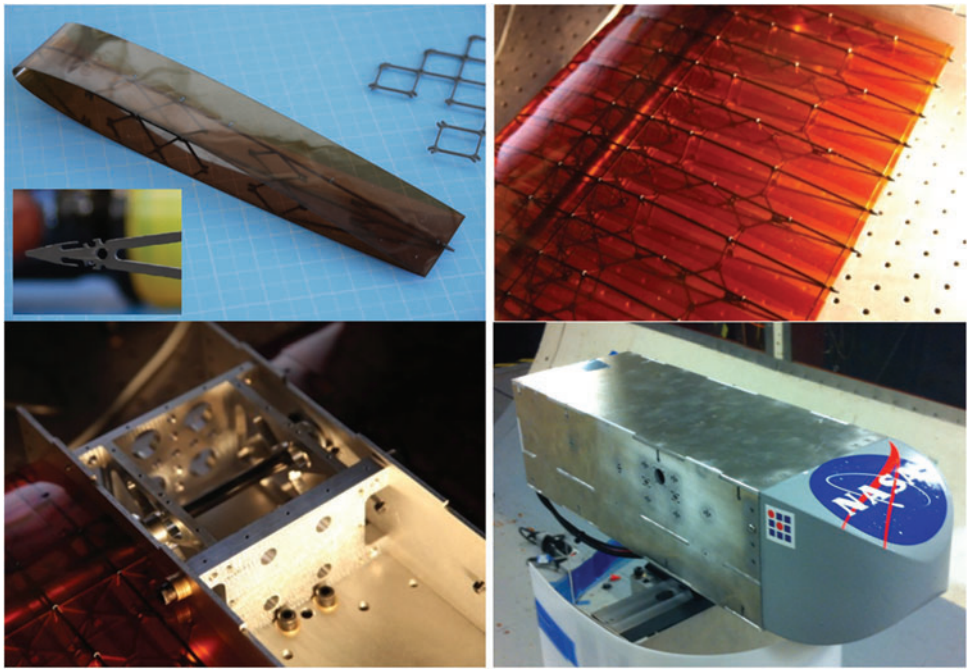

SUPPLEMENTARY FIG. S6. Wing platform details: (clockwise from *top left*) Rib tail feature with hook and detent, single strip of skin on a rib; finished skin with steel retaining pins visible; fuselage external structure with ABS 3D printed nose cone; fuselage internal structure for mounting to six DOF load cells.

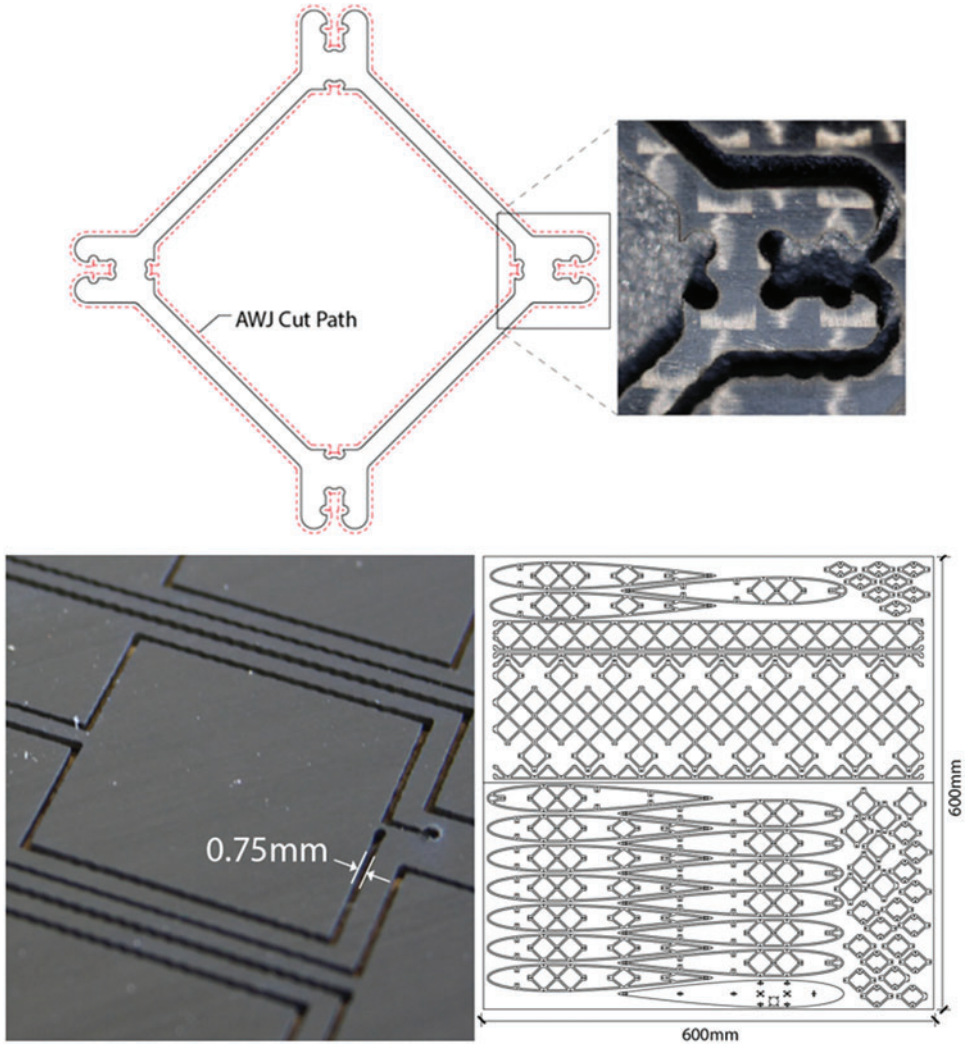

SUPPLEMENTARY FIG. S7. Waterjet cutting details. (*Top*) Cut path is shown in red, offset for kerf width, resulting cut shown to *right*. (*Bottom*) (*Left*) Cut with pneumatically drilled start hole and securing end tab. (*Right*) Sheet layout for one half wing.

SUPPLEMENTARY FIG. S8. Wing boundary condition. Wing tip end cap with bolts to shaft collar, end of torque tube, and zip tie connection to lattice. The lattice acts as a continuous structure between these two boundaries, achieving load transfer and effecting actuation.

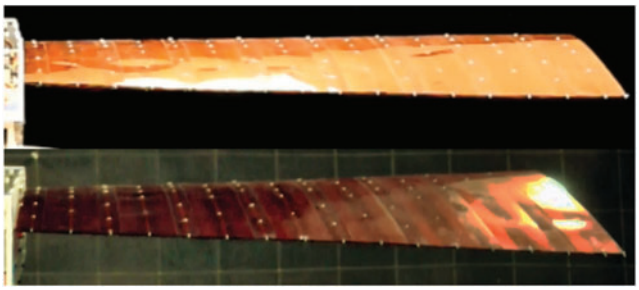

SUPPLEMENTARY FIG. S9. Skin wrinkling under static (*top*), dynamic (*bottom*) loading.

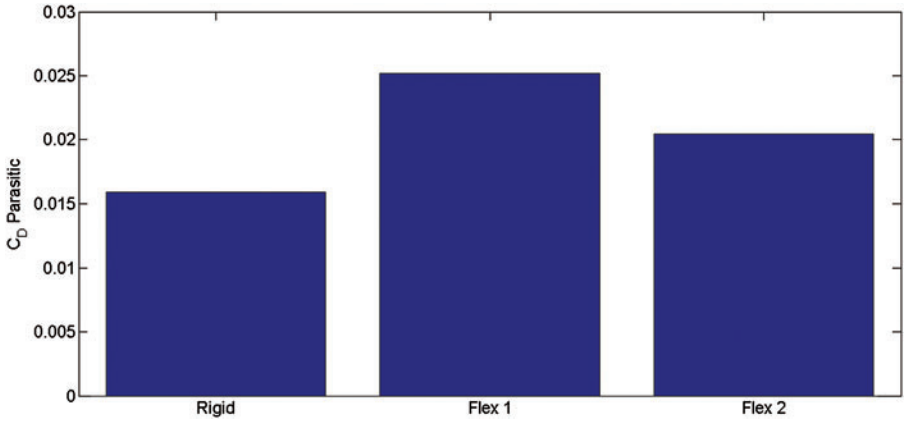

SUPPLEMENTARY FIG. S10. Average of parasitic drag for flat configuration of three models.

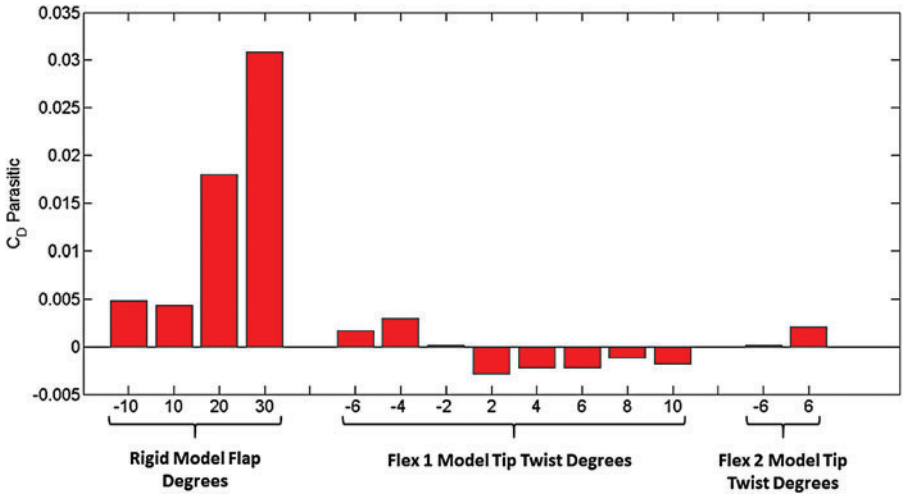

SUPPLEMENTARY FIG. S11. Comparisons of the difference between the flat parasitic drag and the twisted tips or angled flaps.